

# Transient reversible solid oxide cell reactor operation – Experimentally validated modeling and analysis



S. Srikanth<sup>a,\*</sup>, M.P. Heddrich<sup>a</sup>, S. Gupta<sup>b,1</sup>, K.A. Friedrich<sup>a,c</sup>

<sup>a</sup> German Aerospace Center (DLR), Institute for Engineering Thermodynamics, Pfaffenwaldring 38-40, 70569 Stuttgart, Germany

<sup>b</sup> Delft University of Technology, Energy Technology, Leeghwaterstraat 39, 2628CB Delft, Netherlands

<sup>c</sup> University of Stuttgart, Institute of Energy Storage, Pfaffenwaldring 31, 70569 Stuttgart, Germany

## ARTICLE INFO

### Keywords:

SOFC  
SOEC  
Reversible Solid Oxide Cell (rSOC)  
Transient operation  
1-Dimensional reactor model  
Experiment validation

## ABSTRACT

A reversible solid oxide cell (rSOC) reactor can operate efficiently in both electrolysis mode and in fuel cell mode. The bidirectional operability enables rSOC reactors to play a central role as an efficient energy conversion system for energy storage and sector coupling for a renewable energy driven society. A combined system for electrolysis and fuel cell operation can result in complex system configurations that should be able to switch between the two modes as quickly as possible. This can lead to temperature profiles within the reactor that can potentially lead to the failure of the reactor and eventually the system. Hence, the behavior of the reactor during the mode switch should be analyzed and optimal transition strategies should be taken into account during the process system design stage. In this paper a one dimensional transient reversible solid oxide cell model was built and experimentally validated using a commercially available reactor. A simple hydrogen based system model was built employing the validated reactor model to study reactor behavior during the mode switch. The simple design leads to a system efficiency of 49% in fuel cell operation and 87% in electrolysis operation where the

## HIGHLIGHTS

- A hydrogen based system model was built using the validated reactor model.
- A simple system configuration led to a roundtrip storage efficiency of 42%.
- Mode switch from SOFC to SOEC mode possible in 10 s.
- Spatial and temporal temperature gradient in rSOC is the rate of change of reactant inlet temperatures five to ten times slower than the mode switch, a safe initiating mode switch.
- Temporal thermal gradient restricted to 15 K/min.

## 1. Introduction

Higher penetration of intermittent renewable energy sources in the energy mix poses certain critical challenges. The intermittent nature of the renewable sources requires an efficient energy conversion system for energy storage and grid stabilization [1]. Moreover, with reduction in fossil fuel use, alternate synthesis routes for important industrial chemicals have to be developed [2]. Storing electrical energy in form of chemical energy is advantageous due to higher storage capacity and facilitates sector coupling of the energy storage industry with the chemical industry. An rSOC reactor can address the above challenges by operating both as a Solid Oxide Electrolyser Cell (SOEC) and as a Solid Oxide Fuel Cell (SOFC). During the energy storage mode, the electrical energy is converted to chemical form by means of electrolysis. When electrical energy is required, the chemical energy is converted back to electrical energy via fuel cell operation. The high operating

temperatures of SOCs offer many advantages. At higher operation temperatures a greater portion of the energy required for the electrolysis reaction can be supplied as heat when operated in endothermic mode, therefore enabling higher roundtrip efficiency.

To realize such systems, process system analyses have to be performed and complex system architectures have to be investigated. Mottaghizadeh et al. [3] proposed a methane based rSOC system with a downstream methanation process achieving a roundtrip efficiency of 60% operating at 25 bar. Jensen et al. [4] and Monti et al. [5] developed an rSOC system based on a fuel electrode supported rSOC stack design with maximum efficiencies of 60% and 65% respectively. Frank et al. [6] reported an rSOC system based on hydrogen with fuel recirculation and integrated reactor heating whereby a roundtrip efficiency of 51% is reached. The system concepts reported in literature considered highly integrated process system designs to achieve high system efficiencies. Finally, the process system analyses were

\* Corresponding author.

E-mail addresses: [srikanth.santhanam@dlr.de](mailto:srikanth.santhanam@dlr.de) (S. Srikanth), [Sanchit.gupta@dlr.de](mailto:Sanchit.gupta@dlr.de) (S. Gupta).

<sup>1</sup> Permanent address: German Aerospace Center (DLR), Institute of engineering technology, 38-40 Pfaffenwaldring, 70569 Stuttgart, Germany.

Nomenclature		Superscripts	
Symbols	Description, Unit	'	represents quantity entering the control volume
		"	represents quantity leaving the control volume
<i>Latin</i>		a	air electrode side or air flow side
ASR	area specific resistance, $\Omega \text{ m}^2$	bulk	represents the bulk fluid flow in flow chamber
b	effective width of the single repeat unit, m	f	fuel electrode side or fuel flow side
c	specific heat capacity, $\text{J}/(\text{kg K})$	eff	effective
$c_p$	specific heat capacity at constant pressure, $\text{J}/(\text{kg K})$	ic	interconnects
D	diffusion coefficient, $\text{m}^2/\text{s}$	mea	membrane-electrode assembly
E	energy, J	tpb	triple phase boundary
F	Faraday's constant, C/mol		
H	height of the flow channel, m	<i>Subscripts</i>	
h	specific enthalpy, $\text{J}/\text{kg S}$	a	air flow
I	current, A	act	activation process
j	current density, $\text{A}/\text{m}^2$	ae	air electrode
$j_o$	exchange current density, $\text{A}/\text{m}^2$	diffusion	diffusion process
$k^+$	velocity of forward direction of reaction, $\text{mol}/(\text{s m}^2 \text{ bar})$	f	fuel side flow
$k^-$	velocity of reverse direction of reaction, $\text{mol}/(\text{s m}^2 \text{ bar})$	fe	fuel electrode
l	length of the single repeat unit, m	cond	conduction
m	mass, kg	conv	convection
$\dot{m}$	mass flow rate, $\text{kg}/\text{s}$	hor	hydrogen oxidation reaction
M	molecular mass, $\text{kg}/\text{mol}$	ic	interconnect
N	moles, mol	id	thermodynamic conditions or ideal conditions
p	pressure, pa	k	Knudsen diffusion coefficient
	heat flow rate, W	o	oxygen atoms
r	reaction rate, $\text{mol}/(\text{s m}^2)$	ocv	open circuit voltage
R	ideal gas constant, $\text{J}/(\text{mol K})$	ohm	ohmic process
T	temperature, K	op	operation point
U	voltage, V	rad	radiation
x	mole fraction, 1	smr	reverse steam methane reforming reaction
		wgs	reverse water gas shift reaction
<i>Greek letters</i>		<i>Abbreviations</i>	
$\alpha$	convective heat transfer coefficient, $\text{W}/(\text{m}^2 \text{ K})$	ASR	area specific resistance
$\beta$	charge transfer coefficient, 1	CV	control volume
$\Delta$	mathematical operator implying a change in quantity	EOO	equation based object oriented
$\delta$	thickness of a functional layer, m	EIS	electrochemical impedance spectroscopy
$\epsilon$	emissivity of the material, 1	GDC	gadolinium doped ceria
$\epsilon$	porosity of the material, 1	LSCF	lanthanum-strontium-cobalt ferrate
$\gamma$	frequency factor of the electrode reactions, $\text{A}/\text{m}^2$	MEA	membrane-electrode assembly
$\lambda$	conductive heat transfer coefficient, $\text{W}/(\text{m K})$	OCV	open circuit voltage
$\kappa$	equilibrium constant of a reaction, 1	rSOC	reversible solid oxide cell
$\nu$	stoichiometric coefficient of species in a reaction, mol	SOC	solid oxide cell
$\nu$	dynamic viscosity of gas flow, $\text{kg m}/\text{s}^2$	SMR	reverse steam methane reforming reaction
$\rho$	density, $\text{kg}/\text{m}^3$	SOFC	solid oxide fuel cell
$\psi$	tortuosity coefficient, 1	SOEC	solid oxide electrolysis cell
$\sigma$	specific charge conductivity of a the functional layers, $\text{S}/\text{m}$	SRU	single repeating unit
$\sigma_o$	specific conductivity at a reference condition, $\text{S}/\text{m}$	WGS	reverse water gas shift reaction
		3 YSZ	3 mol% Yttrium stabilized zirconia

performed with simplified block models which do not account for the practical limitations of rSOC reactor operation. This can often lead to overestimation of system performances or to operating conditions that would result in reactor failure due to local effects that 0-D models will not reveal. Li et al. [7] quantitatively showed the effect of implementing a detailed reactor model in a SOFC system and its impact on the results compared to process system analysis with 0-D SOFC model. A reduction of system efficiency from 58% to 42% was reported. Magistri et al. [8] performed a similar analysis on a SOFC-Gas turbine hybrid system, where they reported that by using a detailed SOFC model, certain operation points were deemed unfeasible and system

performance was different when constraints were taken into account. A similar assertion is made by D. Oryshchyn et al. [9] in their work on SOFC-Gas turbine hybrid system where a 1-D SOFC model was used for system simulations. Therefore, a higher resolution model is needed for process system analysis to account for the constraints and limitations of the rSOC reactor. In addition, efficient dynamic operation and transient behavior is essential for energy storage system which is challenging even for simple system architectures. The system should be able to follow the transient nature of the intermittent renewable energy sources and time varying energy demand. This would require the system to often switch between the SOFC and the SOEC operation modes.

Therefore, the control system has to ensure a safe operation of the rSOC reactor during the mode switch and also during transient operation in both SOEC and SOFC mode. The process system control should ensure that there is no temperature run away (temperatures which are higher than 100 °C above the average operation temperature) or cold spot (temperatures which are less than 100 °C below the average reactor operation temperature as it can lead to high thermal stresses and ASR) formed in the rSOC reactor due to exothermic and endothermic nature of SOFC and SOEC operation respectively. Therefore to address the above scientific and engineering gaps, a higher resolution rSOC model was built and experimentally validated. A simple hydrogen based rSOC system is built, employing the validated model, to investigate the rSOC reactor behavior during the operation switch between SOFC and SOEC mode. Higher resolution models are available for either dedicated SOFC or SOEC operation. These models are geared towards the optimization of the reactor design or understanding processes on micro scale which are not suitable for system integration. Achenbach et al. [10] reported a three-dimensional transient SOFC model to study different reactor designs, flow configurations and gas manifolds on reactor performance. Menon et al. [11] developed a novel transient model of a SOFC reactor to understand the processes on micro-kinetic scale during transient operation. Laurencin et al. [12] and Ni et al. [13] reported a 2-D steady state SOEC model to analyze the impact of physical characteristics of the reactor and operation conditions on reactor performance. Iora et al. [14] reported 1-D model SOFC to study impact of thermodynamic, flow and physical properties on reactor performance in steady and dynamic operation. Aguirre et al. [15] and Udagawa et al. [16] reported a stationary 1-D model for SOFC and SOEC respectively showing the effect physical characteristics on reactor performance. A dynamic SOFC model for process integration was presented by Salogni et al. [17]. In the domain of a bidirectional operation, a steady state 1-D model of an rSOC reactor can be found in literature. Kazempour et al. presented steady state 1-D rSOC model validated with experimental results from a 4 cm × 4 cm cell. The model can predict the cell performance in both operation modes and study the impact of operation parameters on reactor performance [18]. Jin et al. developed a 2-D transient model for studying the electrochemical behavior during mode switch [19].

The models reported in literature are either specific for SOFC or SOEC operation and rSOC models are not transient or suitable for process system simulations. For these reasons, a detailed dynamic modeling tool of the rSOC reactor is required and a lumped, non-linear 1-D resolution approach was chosen. The model is validated based on experimental results from a 10 cell rSOC stack in SOEC and SOFC operation modes.

Modelling paradigms are presented in Section 2 followed by model implementation in Section 3. The model parametrization and experimental validation is presented in section 4. In section 5, a simple hydrogen based rSOC system is presented in brief. The reactor performance during the switch from SOFC to SOEC operation is discussed.

## 2. Transient 1-D rSOC reactor model

The development of the 1-D model is based on the procedure detailed in the literature [17]. The 1-D model is developed for a single cell in a SOC stack. The single cell is commonly referred to as the single repeat unit (SRU). It is the unit cell representative of the rSOC reactor module located in the middle of an rSOC stack within the reactor module. This assumption is valid as long as the boundary conditions of the SRU are independent. A schematic representation of SRU is shown in Fig. 1. It consists of the fuel chamber, air chamber, membrane-electrode assembly (MEA) and interconnects. A small control volume (CV) of length ‘dx’ along the length of the reactor is considered. The exploded view of the control volume is shown at top of Fig. 1.

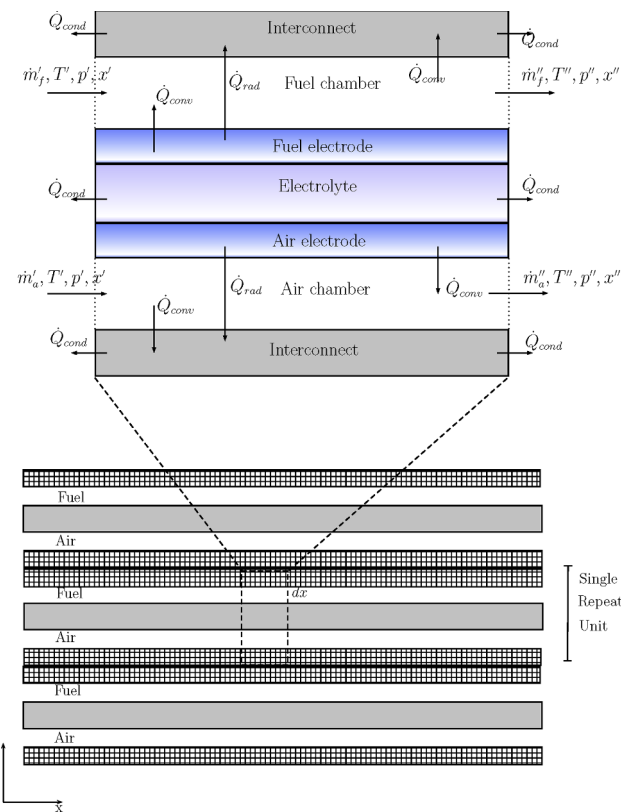


Fig. 1. Schematic of rSOC single repeat unit and control volume of model element of length ‘dx’ discretization.

### 2.1. Assumptions and relevant phenomena

To simplify the model routine, several assumptions are made. The physical processes considered and assumptions made are listed below;

1. Fuel and air chambers are modelled as continuously stirred reactors (CSTR).
2. Pressure drop along the flow channels is considered by assuming laminar flow between two flat plates.
3. Energy accumulation is considered in both solid and gas volumes but mass storage is modelled only for the gas volumes.
4. Convective heat transfer is considered between the solid and gas volumes, radiative heat transfer between the solid parts are modelled. Conductive heat transfer between the solid parts of neighboring control volumes is assumed.
5.  $H_2 - H_2O$  electrochemical reaction is assumed to occur at the electrode electrolyte interface and other reactions such as reverse steam methane reforming (SMR) and reverse water gas shift (WGS) reaction are assumed to occur at the electrode bulk and gas volume.
6. The  $H_2 - H_2O$  electrochemical reaction is assumed to be the main electrochemical reaction. The electrochemical  $CO - CO_2$  reaction is slower than water gas shift (WGS) reactions at SOC operation temperatures as the WGS reaction reaches equilibrium faster. Hence in this model it is assumed that the  $CO - CO_2$  conversion proceeds via WGS reactions and hence electrochemical  $CO - CO_2$  reaction is not considered. Assuming equilibrium the Nernst voltage calculated through  $CO - CO_2$  and  $H_2 - H_2O$  are identical [20].
7. Variation of temperature, pressure and compositions of the gases along height of gas flow channel is neglected. Similarly temperature variation along the z-axis for the solids is neglected.
8. Ideal gas equation of state is used for the gas properties.

## 2.2. Modelling paradigm and governing equations

The model equations are divided into different sub models based on the physical phenomenon present in the control volume. The sub models are (i) gas flow channel sub model, (ii) solid energy storage model, (iii) conductive, convective and radiative heat transfer models, and (iv) electrochemical model. The system of equations for the sub models are provided in detail in the following sections.

### 2.3. Gas flow channel model

The gas flow channel sub model represents the fuel and air flows in the flow channels of the SOC reactor. In this sub model the conservation of species, mass, momentum and energy for the fuel and air flow chamber is modelled. Necessary constitutive equations required for completing the conservative equations are also considered within this sub model. The three reactions considered to occur in the fuel flow chamber are listed in Table 1. The mass and species conservation equations are given by Eqs. (1) and (3) respectively.

$$\frac{dm}{dt} = \dot{m}' - \dot{m}'' + \Delta \dot{m}_o \quad (1)$$

$$\Delta \dot{m}_o = \nu_{O_2,hor} \frac{I}{4F} \quad (2)$$

$$\frac{dm_i}{dt} = \dot{m}_i' - \dot{m}_i'' + bI M_i \sum_{k=1}^3 \nu_{i,k} \Gamma_k \quad i \in H_2, CO_2, N_2, H_2O, CH_4, CO, O_2 \quad (3)$$

In Eqs. (1) and (3), the terms  $\dot{m}$  represents the mass flow rate in kg/s, the superscripts “'” and “''” mark the flows at the in- and outlet of the control volume respectively. In Eq. (1), the  $\Delta \dot{m}_o$  term represents the mass flow rate of oxygen transferred across the electrolyte. The mass rate of oxygen transferred is determined by rate of electrochemical reaction which ultimately depends on the current. For the fuel flow chamber, the term  $\Delta \dot{m}_o$  is positive during the SOFC operation and is negative during the SOEC operation as oxygen is removed from  $H_2O$  and  $CO_2$  in the fuel flow gas mixture. For the air flow chamber, the term  $\Delta \dot{m}_o$  is negative during the SOFC operation and positive during the SOEC operation mode. The mass rate of oxygen transfer is given by Eq. (2). The term ‘I’ in Eq. (2) represents the local cell current which is assumed to be positive for the SOFC operation and negative for the SOEC operation. In Eq. (3), the indices ‘i’ and ‘k’ represents the gas components in the gas mixtures and reaction index respectively. For the modelling work, only seven gas species are considered. Table 2 shows the gas species considered in the present work. The three major reactions that are assumed to occur within the SOC reactor are the electrochemical hydrogen oxidation reaction (hor), the reverse water gas shift reaction (wgs) and the reverse steam methane reforming reaction (smr). The reaction indices ‘k’ for the three reactions are given in Table 1.

The reaction rate for the electrochemical reaction is calculated using the Faraday’s law as given in Eq. (4).

$$\Gamma_{hor} = \frac{J}{2F} \quad (4)$$

The term ‘J’ in Eq. (4) represents the local current density of the SOC. Similar to the cell current, the cell current density is positive for the SOFC operation and negative for the SOEC operation. The current density is calculated by dividing the cell current with effective cell area. The rate of the reverse steam reforming reaction is shown in Eq. (5). Many authors have investigated the kinetics of steam reforming of methane. A brief overview of internal steam reforming and its kinetics is presented by Mogensen et al. [21]. The initial kinetic models of the steam methane reforming reaction over Nickel (Ni) catalysts are provided by Xu and Forment et al. [22]. Their model is a Langmuir-Hinshelwood kinetic model based on experiments performed on Ni

catalysts with Zirconia supports. Achenbach and Reinsche et al. developed a first order kinetic model with respect to methane [23]. A model considering carbon deposition and auxiliary reaction schemes is presented by Wang et al. [24]. A detailed reaction mechanism for methane reforming on Ni/Yttrium stabilized Zirconia (YSZ) catalysts is experimentally studied by Hecht et al., but no kinetic model is presented [25]. A widely used kinetic model for steam reforming is based on a model by Achenbach et al. [23]. Lehnert et al. [26] developed a first order reaction model based on the work of Xu and Forment et al., and it is also commonly used for internal reforming in SOC. Timmerman et al. [27] extended the work of Lehnert et al. [26] and applied the model to predict both internal reforming and methanation. The model parameters were obtained experimentally. Hence, in this work the model proposed in [27] is utilized.

$$r_{smr} = k_{smr}^+ P_{CH_4} P_{H_2O} - k_{smr}^- P_{H_2}^3 P_{CO} \quad (5)$$

The coefficients  $k_{smr}^+$  and  $k_{smr}^-$  are calculated using Eqs. (6) and (7).

$$\kappa_{smr} = \frac{k_{smr}^+}{k_{smr}^-} \quad (6)$$

$$k_{smr}^+ = 2395 \left[ \frac{\text{mol}}{\text{m}^2 \cdot \text{s}} \right] \exp \left( \frac{-231266 \left[ \frac{\text{J}}{\text{mol}} \right]}{RT} \right) \quad (7)$$

where the equilibrium constant ( $\kappa_{smr}$ ) is obtained using the temperature dependent function given below.

$$\kappa_{smr} = 1.0267 \cdot 10^{10} \exp(-0.2513Z^4 + 0.3665Z^3 + 0.581Z^2 - 27.134Z + 3.277)$$

$$Z = \frac{1000[K]}{T}$$

The reverse water gas shift reaction is generally fast and assumed to achieve equilibrium fairly quickly in both directions (see assumption 6). For the SOC model, a first order rate equation is utilized as given in Eq. (8) [13].

$$r_{wgs} = k_{wgs}^+ P_{CO} P_{H_2O} - k_{wgs}^- P_{H_2} P_{CO_2} \quad (8)$$

The coefficients for the forward and reverse reaction are calculated using Eqs. (9) and (10).

$$\kappa_{wgs} = \frac{k_{wgs}^+}{k_{wgs}^-} \quad (9)$$

$$k_{wgs}^+ = 0.0171 \left[ \frac{\text{mol}}{\text{m}^2 \cdot \text{s}} \right] \exp \left( \frac{-103191 \left[ \frac{\text{J}}{\text{mol}} \right]}{RT} \right) \quad (10)$$

The equilibrium constant for the water gas shift reaction ( $\kappa_{wgs}$ ) in Eq. (9) is calculated using the temperature dependent function given below.

$$\kappa_{wgs} = \exp(-0.2935Z^3 + 0.6351Z^2 + 4.1788Z + 0.3169)$$

$$Z = \frac{1000[K]}{T}$$

A simplified momentum balance is employed to evaluate the pressure drop within the flow channel. The momentum balance is obtained by solving the Navier-Stokes equation by assuming a laminar ideal gas flow between infinitely long channels. The pressure drop along the flow

**Table 1**

List of reactions considered within the fuel flow chamber model.

Reactions	Index
$CH_4 + H_2O \rightleftharpoons 3H_2 + CO$	R1
$CO + H_2O \rightleftharpoons H_2 + CO_2$	R2
$H_2O + 0.5O_2 \rightleftharpoons H_2O$	R3

**Table 2**  
Gas species considered in the gas mixture model.

Index	Gas components
1	H <sub>2</sub>
2	CH <sub>4</sub>
3	CO
4	CO <sub>2</sub>
5	H <sub>2</sub> O
6	N <sub>2</sub>
7	O <sub>2</sub>

channel is calculated using Eq. (11).

$$\dot{m}' = \rho' \left( \frac{bH^3(p' - p'')}{12\nu l} \right) \quad (11)$$

The term  $\rho'$  indicates the density of the gas at the inlet of the control volume,  $p'$  and  $p''$  represents the pressure at inlet and outlet of control volume and  $\nu$  represents the viscosity. The equations for the energy balance of the fuel flow channel and the air flow channel are provided in Eqs. (12) and (13) respectively. The energy released due to the reverse water gas shift reaction and reverse steam reforming reaction is considered in the energy balance of the fuel gas flow channel. The electrochemical reaction is assumed to occur at the electrode-electrolyte interface and hence the energy released due to electrochemical reaction is not included in the energy balance of the gas flow channels. The heat transfer due to convection between the solid and fluid medium is considered for both the gas flow channels.

$$\frac{dE}{dt} = \dot{m}'_f h'_f - \dot{m}''_f h''_f + \dot{q}_{conv}^{mea,f} + \dot{q}_{conv}^{ic,f} + r_{smr} \Delta_{smr} h + r_{wgs} \Delta_{wgs} h \quad (12)$$

$$\frac{dE}{dt} = \dot{m}'_a h'_a - \dot{m}''_a h''_a + \dot{q}_{conv}^{mea,a} + \dot{q}_{conv}^{ic,a} \quad (13)$$

The terms  $h$  stands for specific enthalpy in kJ/kg, superscripts “'” and “''” represent the inlet and outlet states, and the subscripts ‘a’ and ‘f’ stand for the air and fuel flow. The terms;  $\dot{q}_{conv}^{mea,f}$  and  $\dot{q}_{conv}^{ic,f}$  in Eqs. (12) and (13) represent the convective heat transfer between the membrane-electrolyte assembly (mea) and gas flow; and the solid interconnects and gas flow respectively. The convective heat transfer is implemented using the heat transfer node explained in Section 2.6.

#### 2.4. Membrane-electrode assembly (MEA) model

The solid electrolyte, fuel electrode and air electrode are modelled as one solid unit. The temperature variation along the height is not considered and the temperature of the MEA is lumped together. Energy accumulation is accounted for and no mass accumulation occurs within the MEA, therefore, only an energy balance is required. The energy balance for the MEA is given by Eq. (14).

$$\rho_{mea} C_{mea} \delta_{mea} bl \frac{dT_{mea}}{dt} = bl r_{hor} \Delta_{hor} h + \dot{q}_{conv}^{mea,f} + \dot{q}_{conv}^{mea,a} + \dot{q}_{rad}^{mea,ic,f} + \dot{q}_{rad}^{mea,ic,a} + \dot{q}_{cond}^{mea} - U_{op} I_{op} \quad (14)$$

The terms,  $\dot{q}_{rad}^{mea,ic,f}$  and  $\dot{q}_{rad}^{mea,ic,a}$ , in Eq. (14) represent the radiative heat transfer between the MEA and interconnects on fuel and air side respectively. The term  $\dot{q}_{cond}^{mea}$  represents the conductive heat transfer along the length of the MEA. The heat transfers are implemented using the heat transfer nodes which are explained in Section 2.6. The last term in Eq. (14) represents the electric power produced or consumed by the cell during SOFC or SOEC operation respectively. The power consumed is assigned a negative sign and power produced is assigned a positive sign. The cell voltage is calculated by the electrochemical model presented in Section 2.4.1.

#### 2.4.1. Electrochemical model

The last term in the energy balance, Eq. (14), corresponds to the work consumed or produced by the reactor. The voltage of the SRU is calculated by the electrochemical model. Electrochemical losses are calculated by resolving each loss mechanism. The rSOC reactor current in SOFC mode is taken as positive value and in SOEC mode as negative value. The cell voltage is calculated using Eq. (15).

$$U_{cell} = U_{id} - (\Delta U_{ohm} + \frac{\Delta U_{act}}{\Delta U} + \Delta U_{diffusion}) \quad (15)$$

$U_{id}$  represents the thermodynamic voltage due to partial pressure of the reactants in the fuel and air chamber [28]. The terms  $\Delta U_{ohm}$ ,  $\Delta U_{act}$  and  $\Delta U_{diffusion}$  in Eq. (15) represent the overpotential due to resistance to charge transport (ohmic loss), overpotential due to electrochemical reaction kinetics (activation loss) and overpotential due to diffusion of reactants to the reaction site (diffusion loss) respectively. The total losses ( $\Delta U$ ) is sum of all the voltage losses.

**2.4.1.1. Ohmic loss.** Ohmic losses account for the voltage drop due to resistance to charge transport. The overpotential due to the ohmic loss is a product of current density and the ohmic component of the Area Specific Resistance (ASR) as given by Eq. (16).

$$\Delta U_{ohm} = j ASR_{\Omega} \quad (16)$$

The term  $ASR_{\Omega}$  is the total resistance to the charge transport and is calculated using Eq. (17). It is equal to the sum of the resistance to oxygen ion transport in electrolyte and electron transport in the electrodes and interconnects. Apart from the functional layers, there are other layers in an rSOC reactor. Additional protective layers are added between the air electrode and the electrolyte to prevent chemical reactions between them. Likewise, protective layers are added between electrodes and interconnect. Moreover, with continuing SOC research new cells/reactors tend to have not just different materials but also different numbers of functional layers. Finding conductivity data for all the materials is difficult. Secondly, the exact description of the materials in the functional layers is not provided and these are mostly a mixture/cermet of varying composition. Hence, the exact data is not available. In light of these realities, the ohmic loss ( $ASR_{\Omega}$ ) is divided into two parts. The first term Eq. (17) takes into account the resistance due to fuel electrode, air electrode and electrolyte with available material data and the second term includes the resistance of the rest of the components such as interconnects, current collectors, protective layers etc.

$$ASR_{\Omega} = \left( \frac{\delta_{fc}}{\sigma_{fc}} + \frac{\delta_{el}}{\sigma_{el}} + \frac{\delta_{ae}}{\sigma_{ae}} \right) + ASR_{reactor} \quad (17)$$

In Eq. (17), the terms  $\delta$  and  $\sigma$  refer to the thickness and conductivity of the functional layers. The term  $ASR_{reactor}$  is a 3rd degree polynomial function of temperature. The coefficients are obtained by fitting the function to the difference between the measured total ohmic resistance from EIS and the calculated ohmic resistance of the functional materials. The temperature dependent relation for conductivity of the functional materials is given by Eq. (18).

$$\sigma_i = \sigma_o / \text{Texp} \left( \frac{-E_{act}}{RT} \right) \quad (18)$$

**2.4.1.2. Activation losses.** Activation losses are typically evaluated using a semi empirical Butler-Volmer equation (BV) [15,29]. The BV is an electrochemical rate kinetic equation similar to a first order rate kinetic equation of chemical reactions. The common form of BV used in SOC modeling based on the assumption of; one-step, single electron transfer process is shown in Eq. (19) [30].

$$j = j_o \left( \exp \left\{ \frac{(1-\beta)FU_{act}}{RT} \right\} - \exp \left\{ \frac{-\beta FU_{act}}{RT} \right\} \right) \quad (19)$$

The term  $j_0$  is the exchange current density. It is the current density always exchanged back and forth at equilibrium state when no reaction takes place. The value of the symmetry factor ' $\beta$ ' varies between 0.25 and 0.5 [31,32]. The symmetry factor indicates how the activation energies of forward and backward reaction are affected by the voltage. Using  $\beta = 0.5$  in Eq. (19), the equation can be simplified to an inverse hyperbolic sine function. The inverse hyperbolic simplification of BV provides higher accuracy for a wide range of current densities for  $\beta \leq 0.7$  [30]. For the model, the activation loss is calculated using the simplified BV as shown in Eq. (20).

$$U_{\text{act}} = \frac{RT}{0.5F} \sinh^{-1} \left( \frac{j}{2j_0} \right) \quad (20)$$

The exchange current density for the fuel electrode and oxygen electrode are given by Eqs. (21) and (22) respectively. The partial pressure of the species used in equation Eqs. (21) and (22) are the values at the triple phase boundary (reaction site).

$$j_{0,fe} = \gamma_{fe} \left( \frac{P_{H_2}^{\text{tpb}}}{P} \right)^m \left( \frac{P_{H_2O}^{\text{tpb}}}{P} \right)^n \exp \left( \frac{-E_{\text{act},fe}}{RT} \right) \quad (21)$$

$$j_{0,ae} = \gamma_{ae} \left( \frac{P_{O_2}^{\text{tpb}}}{P} \right)^k \exp \left( \frac{-E_{\text{act},ae}}{RT} \right) \quad (22)$$

**2.4.1.3. Diffusion losses.** Diffusion losses are due to resistance to mass transport of gases from flow chambers to the reaction sites. The electrochemical reactions occur at the electrolyte-electrode interfaces. The reactants must therefore diffuse to the reaction sites through the porous electrodes. The electrochemical reaction at the reaction sites leads to the concentration gradient across the electrodes for both reactants and products which drive the diffusion transport mechanism. Fick's Model, the Stefan-Maxwell Model and the Dusty Gas Model (DGM) are commonly used for modelling the mass transport in SOC reactors [20,33,34]. An overview of performance of the three different models is presented by Suwanwarangkul et al. [33]. DGM has the highest accuracy but it is difficult to obtain an analytical solution and therefore it requires numerical solution. This adds to computational effort/time which is especially unfavorable for transient models [35]. The Stefan-Maxwell model omits Knudsen diffusion which is significant SOC's operation in low pressure regions from 1 to 3 bar [36]. Hence, in this work an extended Fick's law model with Knudsen diffusion is employed, assuming  $\frac{dp}{dz} = 0$ , is used for calculating the concentrations at the reaction sites. The diffusion losses are calculated using Eqs. (23) and (24).

$$U_{\text{diffusion},fe} = -\frac{RT}{2F} \left( \frac{x_{H_2}^{\text{tpb}} x_{H_2O}}{x_{H_2O}^{\text{tpb}} x_{H_2}} \right) \quad (23)$$

$$U_{\text{diffusion},ae} = -\frac{RT}{4F} \left( \frac{x_{O_2}^{\text{tpb}}}{x_{O_2}} \right) \quad (24)$$

The gas concentrations at the reaction site are calculated using Eqs. (25)–(32). The transport equation assuming  $dp/dz = 0$  reduces to by Eq. (25).

$$N_i = \frac{P}{RT} \left( -D_i^{\text{eff}} \frac{dx_i}{dz} \right) \quad (25)$$

The effective gas diffusion term, " $D_i^{\text{eff}}$ " in Eq. (25) is evaluated based on the multicomponent gas diffusion. For the fuel electrode, a ternary gas system comprising of  $H_2$ ,  $H_2O$  and  $N_2$  is considered. The gas components CO and  $CO_2$  are not considered since it is assumed that  $H_2$ - $H_2O$  is the main electrochemical reaction and  $H_2$ ,  $H_2O$  are the main diffusing gases. The WGS and SMR reactions take place relatively far from the TPB at the electrode surface and not present in the electrode bulk. The effective

diffusion coefficient for hydrogen is given by Eq. (26).

$$\frac{1}{D_{H_2}^{\text{eff}}} = \frac{1}{D_{H_2,K}^{\text{eff}}} + \frac{1}{D_{H_2-N_2}^{\text{eff}}} + \left( \frac{1}{D_{H_2-H_2O}^{\text{eff}}} - \frac{1}{D_{H_2-N_2}^{\text{eff}}} \right) (1-x_{N_2}) \quad (26)$$

A similar equation can be obtained for evaluating the effective diffusion coefficient of water. The mass transport of hydrogen and water are coupled to the current density. Integrating Eq. (25) under the boundary condition  $x_{i|z=0} = x_i^{\text{bulk}}$  results in Eqs. (27) and (28) for  $H_2$  and  $H_2O$  mole fractions respectively.

$$x_{H_2}^{\text{tpb}} = x_{H_2}^{\text{bulk}} - \frac{jzRT}{2FD_{H_2}^{\text{eff}}P} \quad (27)$$

$$x_{H_2O}^{\text{tpb}} = x_{H_2O}^{\text{bulk}} + \frac{jzRT}{2FD_{H_2O}^{\text{eff}}P} \quad (28)$$

To evaluate the oxygen diffusion on the cathode side, the binary diffusivity method is employed. A constant pressure along the electrode thickness is assumed. The oxygen mass transport is given by Eq. (29).

$$N_{O_2} = \frac{P}{RT} \left( -D_{O_2}^{\text{eff}} \frac{dx_{O_2}}{dz} + x_{O_2} \delta_{O_2} N_{O_2} \right) \quad (29)$$

The equations to calculate the effective diffusion coefficient of oxygen and  $\delta_{O_2}$  is provided by Eqs. (30) and (31) respectively.

$$D_{O_2}^{\text{eff}} = \left( \frac{1}{\{D_{O_2,N_2}^{\text{eff}} + D_{O_2,K}^{\text{eff}}\}} \right)^{-1} \quad (30)$$

$$\delta_{O_2} = \frac{D_{O_2,k}^{\text{eff}}}{(D_{O_2,N_2}^{\text{eff}} + D_{O_2,K}^{\text{eff}})} \quad (31)$$

Similar to hydrogen and water, the oxygen mass transport flux is coupled to the current density via Faraday's law. Substituting the relation for oxygen mass transport flux in Eq. (29) and integrating with the limit  $x_{i|z=0} = x_i^{\text{bulk}}$ , an equation for evaluating the mole fraction of oxygen at the reaction sites is obtained as shown in Eq. (32).

$$x_{O_2}^{\text{tpb}} = \frac{1}{\delta_{O_2}} \left( \frac{1}{\delta_{O_2}} - x_{O_2}^{\text{bulk}} \right) \exp \left( \frac{jRT\delta_{O_2}z}{4FD_{O_2}^{\text{eff}}P} \right) \quad (32)$$

The term  $D_{i,K}$  in Eqs. (26), (30) and (31) stands for the Knudsen diffusion of the gas species and is evaluated from the kinetic theory of gases using Eq. (33). In Eq. (33), the term  $d_p$  and  $\pi$  stands for the pore diameter and collision integral respectively.

$$D_{i,K} = \frac{d_p}{3} \sqrt{\frac{8RT}{\pi M_i}} \quad (33)$$

The binary diffusion coefficients are calculated based on the Lennard-Jones potential and Chapman-Ernskog diffusion theory. The effective diffusion coefficient (both molecular and Knudsen) takes into account the porosity and tortuosity of the electrodes. It is calculated using Eq. (34). The terms  $\epsilon$  and  $\psi$  in Eq. (34) indicate the porosity and tortuosity of the electrodes respectively.

$$D^{\text{eff}} = D \left( \frac{\epsilon}{\psi} \right) \quad (34)$$

## 2.5. Interconnect

Interconnects are modelled as a lumped solid component. Only thermal energy accumulation is considered in interconnects. The resistance due to charge transport is considered in the electrochemical model in the previous section.

$$\rho_{ic} c_{ic} \delta_{ic} bl \frac{dT_{ic}}{dt} = \dot{q}_{conv}^{ic,f} + \dot{q}_{conv}^{ic,a} + \dot{q}_{rad}^{mea,ic,f} + \dot{q}_{rad}^{mea,ic,a} + \dot{q}_{cond}^{ic} \quad (35)$$

## 2.6. Heat transfer models

Three major heat transfer phenomena are considered in the model. The convective heat transfer between gases and solids, conductive heat transfer between solids and radiative heat transfer between the solids are modelled. The convective heat transfer occurs between the solid (MEA and interconnect) and gas flows (fuel and air flow). The convective heat transfer coefficient ( $\alpha$ ) is obtained by assuming a constant Nusselt number for laminar flow between infinitely long plates. This assumption results in a constant value for the heat transfer coefficient. Similar assumptions can be found in literature [15,17,37–39]. The convective heat transfer is evaluated using Eq. (36).

$$\dot{q}_{\text{conv}} = \alpha_i b \Delta T \quad (36)$$

The radiative heat transfer is important in a solid oxide cell due to high operation temperature. Detailed studies were performed on the importance of radiative heat transfer effects on the cell performance [12,40–42]. The radiative heat transfer is evaluated between the solid interconnects (air and fuel side) and solid MEA using Eq. (37). The term  $\epsilon_i$  in Eq. (37) refers to the emissivity of the solid functional layers.

$$\dot{q}_{\text{rad}} = \frac{\left( 5.67 \cdot 10^{-8} \left[ \frac{\text{W}}{\text{m}^2 \text{K}^4} \right] b \epsilon_{\text{mea}} \epsilon_{\text{ic}} (T_{\text{mea}}^4 - T_{\text{ic}}^4) \right)}{(\epsilon_{\text{mea}} + \epsilon_{\text{ic}} - \epsilon_{\text{mea}} \epsilon_{\text{ic}})} \quad (37)$$

Finally the conductive heat transfer occurring in the solid structure along the length of the cell and between the MEA and interconnect is evaluated using Eq. (38). The thermal conductivity of the solid material ( $\lambda_i$ ) in Eq. (38) is obtained from literature (refer Table 4 in Section 4.1).

$$\dot{q}_{\text{cond}} = \lambda_i l \Delta T_i \quad (38)$$

## 3. Modelica implementation

The model equations are implemented in the equation based object oriented language Modelica. The commercial editor Dymola from Dassault systems is used and can also work with OpenModelica which is an open source editor. Different components of the model that are re-used can be modelled as separate objects. These objects can be called upon when required. Each subsystem described above forms an object of its own. There are four main objects based on the subsystems; (i) fuel flow chamber, (ii) air flow chamber, (iii) MEA and (iv) interconnect. Additionally, three objects are defined based on the three heat transfer mechanisms; (i) conductive heat transfer, (ii) radiative heat transfer, (iii) convective heat transfer. The subsystems along with the heat transfer objects forms the control volume that simulates an SRU but under the assumption that the SRU behaves like a CSTR reactor. To get a more realistic model, the control volume is repeated 'n' times based on the required discretization to model a plug flow type SRU. The gas flows are connected in series according to the flow direction. The MEAs are connected as parallel electrical circuits. This assumption is made because the electrode surfaces are almost equipotential surfaces. The system of equations is solved for the boundary conditions Eqs. (39) and (40). Local current density, local thermodynamic voltage (due to local conditions), local compositions, local temperature, local losses etc. are resolved accordingly.

$$U_{i=1 \dots n} = U_{\text{op}} \quad (39)$$

$$I_{\text{op}} = \sum_{i=1}^{i=n} I_i \quad (40)$$

## 4. Parameterization and model validation

The 1-D rSOC model was implemented for a commercially available rSOC reactor. The reactor is a ten layer stack based on an Electrolyte Supported Cell (ESC) framework and with an open air manifold design.

**Table 3**

Physical parameters of the rSOC reactor used for model validation.

Functional layer	Material	Thickness/ $\mu\text{m}$	Porosity
Fuel electrode contact	Ni	15	0.4
Fuel electrode	Ni-GDC	15	0.4
Electrolyte	3YSZ	90	0
Air electrode	LSCF	25	0.4
Air electrode contact	LSCF	30	0.4

The physical characteristics of the rSOC reactor are provided in Table 3. The rSOC reactor was experimentally characterized at different operating conditions and the model was validated using the experimental results. Steady state and dynamic U(j) characteristic curves were generated for both SOFC and SOEC operation modes. For steady state measurements the reactant flow to the rSOC reactor is set to maintain a constant reactant conversion at each current density. Whereas in dynamic measurements the reactant flow is constant and the current density is changed leading to increasing reactant conversion values with increasing current density. Electrochemical impedance spectroscopy (EIS) measurements were performed at OCV at different temperatures and pressures to quantify ohmic resistance. The reactor pressure and furnace temperature were varied from 1.4 bar to 8 bar and 750 °C to 850 °C respectively in both SOFC and SOEC mode. The reactant conversion was varied in the range of 55–85 % in SOFC mode and 60–75% in SOEC mode. EIS measurements were performed at OCV conditions at different temperatures from 700 °C to 850 °C. The cell voltage was measured for the center SRU which is the fifth unit in a ten layer SOC reactor and was used for validation of the model. Further details on the experiments and analysis of the experimental results are presented by Santhanam et al. [28] and Riedel et al. [43].

### 4.1. Model input parameters and fitting parameters

The input parameters provided to the model by the user are listed in Table 4. The activation energies for the charge transport in different functional layers were obtained from literature [20,44,45], as well as the thermomechanical properties of the functional layers [14,15,32].

The other model parameters such as the activation energies for the electrodes, pre-exponential factors for exchange current densities, tortuosity factor etc. were obtained by fitting the model to the activation and diffusion losses obtained from the experimental results. The values of these parameters are given in Table 5. The fitted values lie within the range of values for activation energies and pre-exponential factors given in literature. The values for activation energies and pre-exponential factor should be taken at a face value and do not exactly describe the electrochemical properties of the electrode as they are only a fit value.

In order to arrive at more precise values for activation energies and pre-exponential factors, a thorough detailed method as described by Leonide et al. [46,47] is imperative. The method proposed by Leonide et al. requires an extensive list of experiments and analysis of the experiments using the distribution of relaxation time method (DRT) and finally estimating the parameters using equivalent circuits. Application of the method proposed by Leonide et al. is challenging for rSOC reactor with ten layers. Additionally, SRUs in an rSOC reactor have an effective area larger than button cells used in such studies. Hence for this model, a simpler non-linear curve fit method was utilized to estimate the parameters.

The term  $ASR_{\text{reactor}}$  in Eq. (17) is temperature dependent and is derived by fitting a polynomial to the difference between the total ohmic resistance measured from EIS and the combined resistance of the anode, cathode and electrolyte calculated using material properties. The temperature dependent polynomial function of  $ASR_{\text{reactor}}$  is provided in Eq. (41). The values of the coefficients in Eq. (41) are provided in Table 5.

**Table 4**  
Material and physical input parameters used for the 1-D model.

Parameters	Value	Unit
<i>Fuel electrode</i>		
$\sigma_0$	$95 \cdot 10^6$	S K/m
$E_{act}/R$	-1150	K
<i>Air electrode</i>		
$\sigma_0$	$42 \cdot 10^6$	S K/m
$E_{act}/R$	-1200	K
<i>Electrolyte</i>		
$\sigma_0$	$5.15 \cdot 10^{-7}$ *	SK/m
$E_{act}/R$	-10300	K
<i>Physical dimensions</i>		
Length of cell	0.090	m
Width of cell	0.142	m
Height of flow channel	0.001	m
<i>Membrane electrolyte assembly (MEA)</i>		
Heat capacity	500	J/(kg K)
Emissivity	0.8	1
Thermal conductivity	2	W/(m K)
Density	6000	kg/m <sup>3</sup>
<i>Interconnect</i>		
Heat capacity	800	J/(kg K)
Emissivity	0.1	1
Thermal conductivity	25	W/(m K)

**Table 5**  
Fitting parameters obtained for the 1-D model.

Parameter	Fitted value	Unit
$\gamma_{fe}$	$1.33 \cdot 10^6$	A/m <sup>2</sup>
$\gamma_{ae}$	$1.14 \cdot 10^7$	A/m <sup>2</sup>
$E_{act,fe}$	52.198	kJ/mol
$E_{act,ae}$	66.239	kJ/mol
m	-0.1	1
n	0.33	1
k	0.22	1
$\psi_{fe}$	6.8166	1
$\psi_{ae}$	5.1847	1
$A_1$	0.02348	$\Omega \text{ m}^2$
$A_2$	$-6.81903 \cdot 10^{-5}$	$\Omega \text{ m}^2/\text{K}$
$A_3$	$5.47259 \cdot 10^8$	$\Omega \text{ m}^2/\text{K}^2$
$A_4$	$-1.6207 \cdot 10^{-11}$	$\Omega \text{ m}^2/\text{K}^3$

$$ASR_{reactor} = A_1 + A_2T + A_3T^2 + A_4T^3 \quad (41)$$

## 4.2. Model validation

### 4.2.1. Validation in SOFC operation mode

The 1-D rSOC model was validated against the experimental measurements with both steady state and dynamic U(j) characteristic curves. The validation was performed for conversion ratio of 55% and 85%. The lower conversion ratio of 55% is the minimum value that is expected to be reached in the system operating conditions. The higher conversion ratio of 85% is used for the system consideration during SOFC operation and hence is chosen for validation. The comparison of steady state U(j) characteristic curves simulated by the model with the steady state U(j) measurements from experiments in SOFC mode is shown in Fig. 2a and 2c. The temperature near the center of the SRU (0.5 times length of the SRU) and close to exit of the SRU (0.75 times the length of the SRU) as measured during the experiment and predicted by the model is shown in Fig. 2b and d.

The model prediction is in reasonable tolerance with the measurements at both low and high pressures. For the steady state SOFC

measurements, the model was able to predict the experimental results with maximum error of 2 percentage points of the total value for fuel conversion of 55% and a maximum error of 4 percentage points of the total value for experiments with fuel conversion of 85%. In Fig. 2a, at 85% conversion and 1 bar pressure, the deviation of the model prediction from experimental value is high at lowest current density of 750 A/m<sup>2</sup>. This is due to an anomaly in the experimental value as the voltage measure at 750 A/m<sup>2</sup> is almost equal to the voltage measured at 1200 A/m<sup>2</sup>. The reason for the experimental anomaly is discussed in detail by Santhanam et al. in [28]. The validation of the 1-D model with SOFC dynamic U(j) measurements at all pressures is shown in Fig. 3. A maximum error of 2 percentage points of the total value for the model with measurements at current densities above 500 A/m<sup>2</sup> is observed. At current densities lower than 500 A/m<sup>2</sup>, the discrepancy between the measured values and the ones generated by the model is high. Two possible reasons for this error are discussed below:

1. At these current densities, the activation overpotential loss is expected to be the dominating loss mechanism which is computed using the BV equation. Hence, the error in the model could be either due to the approximation of the BV equation to a hyperbolic function. Though the effect of approximation is not seen in the other U(j) measurements simulated using the model. For example, within the simulation of steady state U(j) measurements as shown in Fig. 2, the model can predict the voltage at current density lower than 500 A/m<sup>2</sup> with reasonable error percentage of 2 points to the experimentally measured value. Also, a good fit at lower current densities can be observed for the simulated dynamic U(j) measurements in the SOEC operation mode shown in Fig. 4 which will be discussed later.
2. The deviation could be due to an anomaly in the experiments. Though dry fuel was used, a small percent (less than 0.01%) of water vapor is expected to be present in the feed gas as impurity. This can be calculated from the OCV of 1.3 V measured during the forward sweep. During the forward sweep (current density is increased from 0 A/m<sup>2</sup> to 2000 A/m<sup>2</sup>), the voltage produces an arching behavior at low current density (till 500 A/m<sup>2</sup>). This could be due to low concentrations of water evolution at low current densities which are then quickly flushed out by the incoming gas flow, therefore, resulting in a “dry” condition on the fuel electrode side. As the current density is increased, due to the prevalent “dry” condition on the fuel side, a higher voltage is measured. Once a current density of 500 A/m<sup>2</sup> is reached, sufficient water is generated on the fuel side which is still present in the flow channel, and hence a drop in voltage is observed as expected behavior for fuel cell operation. During the back sweep (current density is decreased from 2000 A/m<sup>2</sup> to 0 A/m<sup>2</sup>), it can be observed that a voltage of 1.2 V is observed at 0 A/m<sup>2</sup> compared to 1.3 V during forward sweep. Moreover, the arching behavior of the voltage is not seen at lower current densities during back sweep. Sufficient water is produced by the time the forward sweep ends, which is then retained in the electrode pores and is not completely flushed out. This entrapped water in the pores is present during the back sweep, resulting in the observed behavior. In the model, the complex phenomenon behind the observed effect is not captured.

### 4.2.2. Validation in SOEC operation mode

The model was validated in SOEC mode with both steady state and dynamic measurements. In Fig. 4, the performance of the model compared to the steady state experimental measurements in SOEC mode under two different pressure conditions can be observed. The model has an absolute maximum error of 2 percentage points of the total value with the measurements.

Similarly the performance of the 1-D model against dynamic U(j) measurements in SOEC operation mode is shown in Fig. 5 for two different pressures. An accurate prediction of the model is obtained with a slight deviation in the range of 0.5% is observed at higher current

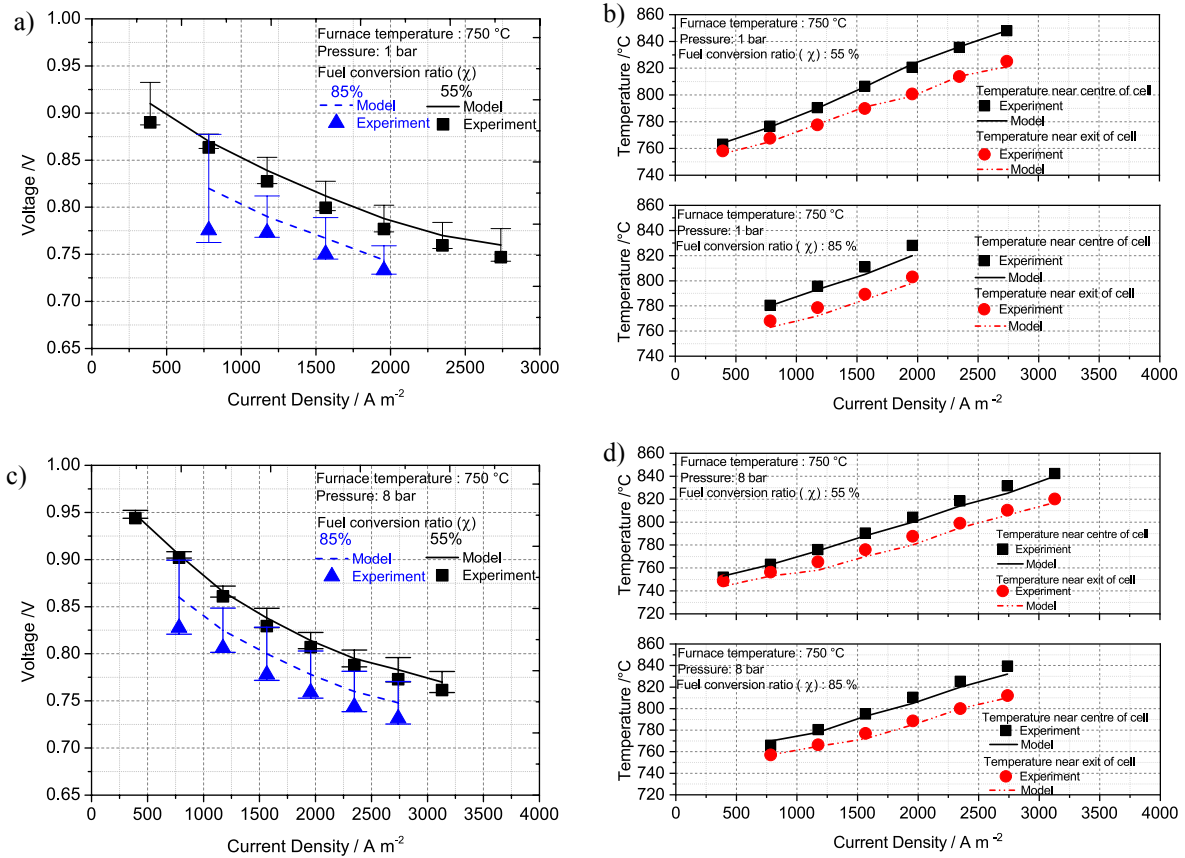


Fig. 2. Experimental and model results of steady state (a) U(i) in SOFC mode at 1 bar, (b) T(i) at 55% (top) and 85% (below) fuel conversion and 1 bar, (c) U(i) in SOFC mode at 8 bar, (d) T(i) at 55% (top) and 85% (below) fuel conversion and 8 bar.

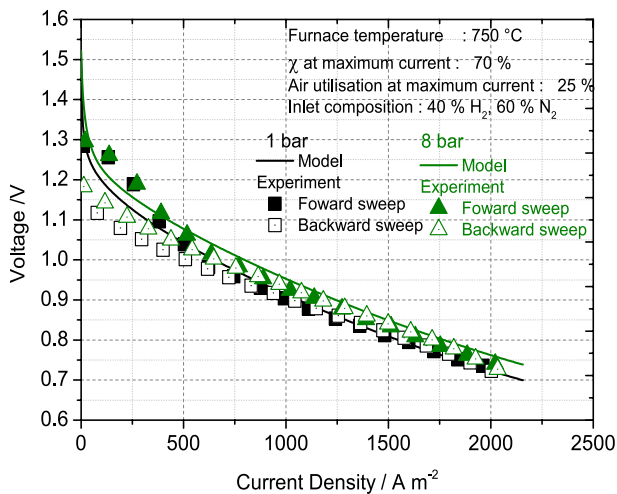


Fig. 3. Validation of 1-D model with dynamic measurements in SOFC mode.

densities.

### 5. Transient operation study of rSOC reactor

A simple hydrogen based rSOC system model is built utilizing the validated model to understand the reactor behavior during the operation mode switch. The variation of the temperature profile within the rSOC during the mode switching is studied for different conditions. This is essential to ensure the safety of an rSOC system and to prevent failures of the cell, rSOC reactor and therefore the rSOC system itself.

### 5.1. System description

In Fig. 6, the process flow diagram of the hydrogen based rSOC system is provided indicating the boundary conditions before and after the reactor at the design SOFC and SOEC steady state operation point. The assumptions made for the system simulation are presented in brief below. A detailed overview of the assumptions is presented in [28].

- Symmetric operation of the r-SOC system is considered. The duration of the charging process (SOEC process) is equal to the duration of discharging process (SOFC process).
- The charge transferred during the SOFC operation (oxygen ions from air to fuel side) is equal to the charge transferred during the SOEC operation (oxygen ions from fuel to air side).
- Assumptions 1 and 2 result in equal current during the SOFC and SOEC operations.

In the SOFC operation mode, hydrogen is supplied to the rSOC reactor after being preheated to the required inlet temperature. Similarly, ambient air is supplied to the air electrode chamber after being preheated to the required inlet temperature. The outlet streams of the reactor are fed to the heat recovery system where it supplies the heat required for preheating the inlet streams. In the SOEC operation, the water required for electrolysis is fed to the heat recovery unit where it is converted to steam and preheated to the required inlet temperature. Hydrogen from the hydrogen storage tank is premixed with the steam to prevent nickel oxidation in the fuel electrodes. Ambient air is supplied as sweep gas to flush the produced oxygen. It is preheated to the inlet temperature in the heat recovery unit. The reactant streams are fed to a preheater (electric) to supply the excess heat for endothermic electrolysis reaction or for cases where the required inlet temperature is

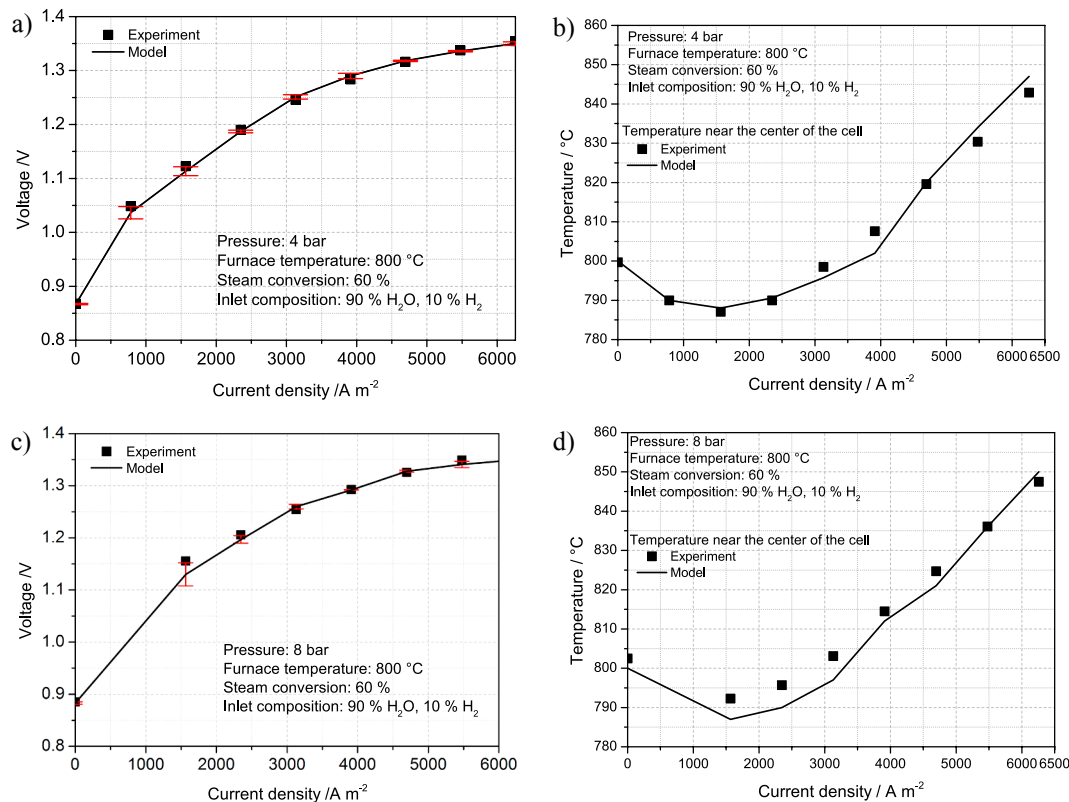


Fig. 4. Experimental and model results of steady state (a) U(i) in SOEC mode at 4 bar, (b) T(i) in SOEC mode at 4 bar, (c) U(i) in SOEC mode at 8 bar, (d) T(i) in SOEC mode at 8 bar.

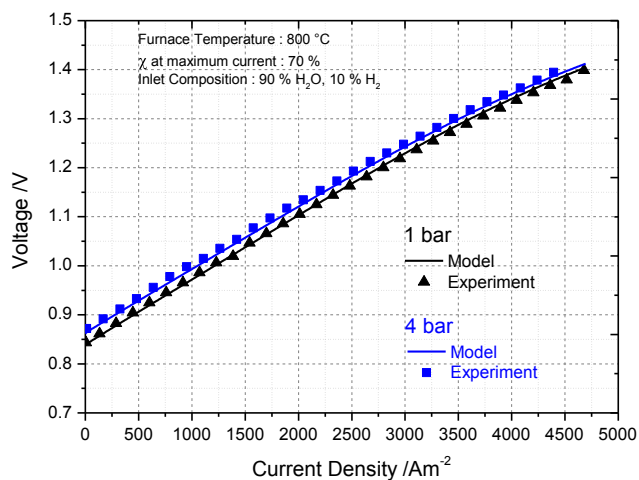


Fig. 5. Comparison of 1-D model prediction versus dynamic measurements at different pressures in SOEC with 90% H<sub>2</sub>O and 10% H<sub>2</sub>.

not reached. The reactor outlet streams of SOEC operation are then fed to the heat recovery unit where they are cooled and heat is used for preheating the inlet streams. Finally hydrogen is separated from unreacted water and stored in a hydrogen tank. The system employs the validated 1-D rSOC reactor model described in Section 4.

### 5.2. Transient operation simulation descriptions

A transient simulation was performed for the system operating condition. The simulation was performed to understand the challenges and potential problems that should be addressed when switching between designed SOEC and SOFC operation points. For every simulation, the behavior of the temperature profile along the flow direction during

the transient operation is studied. The study aims to identify whether any undesirable thermal spikes or rapid increase or decrease of temperature can occur within the SRU during the transient behavior. Such behavior is dangerous for the longevity of the rSOC reactor and can potentially lead to the failure of the rSOC system. In moving from SOFC to SOEC operation, the inlet conditions such as the inlet temperature and composition of the reactants change. Hence, in this analysis, the focus is only on the transient behavior of the rSOC reactor for different rates at which the inlet conditions change from SOFC steady state operating point to the SOEC steady state operating point. In this study, the dynamic behavior and transient response of the balance of plant (BoP) components are not considered. The simulations were performed for different conditions that were identified based on the expected rSOC system operation. The simulations were run for three operation hours at the steady state operating point in SOFC mode before it is switched to the steady state SOEC operating point. The simulation runs for an additional three operation hours at the steady state operating point in the SOEC mode. In total, the rSOC system operation is simulated for duration of six hours each, for each of the transition strategies considered in this study. In the graphs below, the time of switch from the SOFC to SOEC mode is the reference time (at 0 min in the graphs). Hence, the SOFC operation hours are negative and SOEC operation hours are positive.

#### 5.2.1. Simulation #1- step change at SOC inlet conditions and operation

The inlet conditions of the reactants entering the rSOC reactor and the operation mode were immediately switched from the SOFC design operating point to the SOEC design operating point. Though this is quiet challenging from an actual operational point of view, it is expected that future rSOC systems can switch from SOFC to SOEC mode immediately. Hence, it is interesting to understand the effects of such variation on the processes within the rSOC reactor. The steady state operating points in the SOFC and SOEC modes are given in Table 6. The inlet temperature

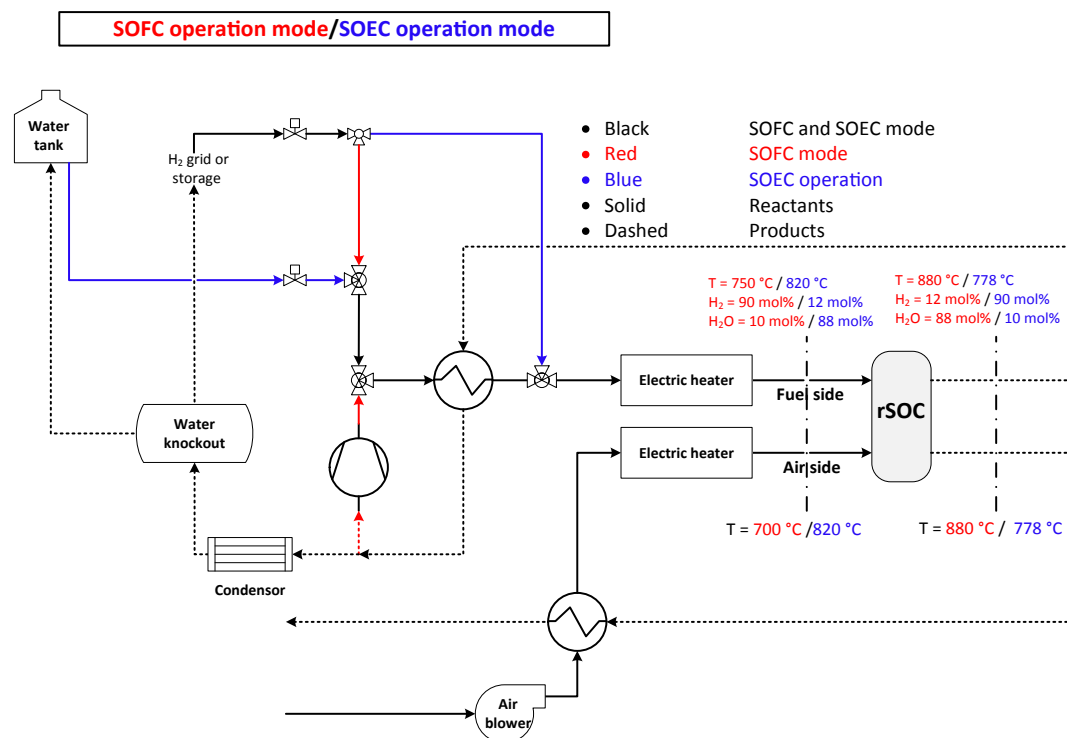


**Fig. 6.** Process flow scheme of a hydrogen based rSOC system showing the inlet and outlet boundary conditions of the rSOC reactor at the design steady state operation points. The black lines are common for both SOFC and SOEC mode. Blue and red lines are active only during the SOEC and SOFC mode respectively. (For interpretation of the references to colour in this figure legend, the reader is referred to the web version of this article.)

of the reactants entering the fuel and air chamber are varied as a step function from 750 °C to 820 °C and 700 °C to 820 °C respectively. Likewise the reactant composition at inlet of the fuel chamber is from 90 mol% hydrogen and 10 mol% water to 12 mol% hydrogen and 88 mol% water as a step function. Such variations are possible only if the fluid flow response and heating up of the gases are fast enough. The current density for the rSOC reactor was varied as a step function from 2500 A/m<sup>2</sup> in SOFC mode to -2500 A/m<sup>2</sup> in SOEC mode. The variations of the inlet parameters to the rSOC reactor from the SOFC to SOEC operation mode are shown in Fig. 7.

### 5.2.2. Simulation #2- equal ramp duration for all parameters at SOC inlet conditions

The second situation considered was the variation of the inlet reactants' composition and temperature from SOFC operation to SOEC operation as a ramp function. The system was gradually switched from SOFC operation to SOEC operation. The duration of change for all the key parameters such as inlet temperature, composition, and current density were equal. A fast ramp change of process parameters, from the steady state SOFC condition to steady state SOEC condition, in a duration of one minute was implemented. The variation of the key inlet parameters from the steady state SOFC operation to steady state SOEC operation is shown in Fig. 8.

### 5.2.3. Simulation #3- ramp function with lagged temperature change at SOC inlet

In this simulation run, the key inlet conditions were varied from the steady state SOFC operation to steady state SOEC operation as a ramp function. Unlike in Simulation #2, the duration of the change between the two modes was not equal for all the key parameters. The duration of variation of the inlet reactant compositions (and mass flows) and the current density between the SOFC operation point and SOEC operation point were equal. The duration of the change of inlet temperature of the reactants entering the rSOC reactor was ten times slower than that of the current density and composition. This was done to study the effect

of rate of change of inlet temperature on the temperature profile in the rSOC reactor. The rate of change of the inlet conditions from SOFC operation to SOEC operation is depicted in Fig. 9.

## 5.3. Results and discussions

### 5.3.1. rSOC system and reactor behavior under steady state conditions

The system performance and key operational parameters at the design steady state points in SOFC and SOEC mode are provided in Table 6. In the SOFC mode, the single pass fuel conversion of 86% was set in the SOC reactor. The fuel exhaust recycle ratio was fixed at 11% resulting in a total system fuel conversion of 90% at design steady state operating point. The system operates at a chemical-to-electric conversion efficiency (1st law, LHV based) of 49.4% in SOFC mode. A

**Table 6**

Steady state operation points in SOFC and SOEC mode from hydrogen based system.

Parameter	Value	Unit
<i>SOFC operation mode</i>		
Fuel side inlet temperature	750	°C
Air side inlet temperature	700	°C
Fuel side outlet temperature	880	°C
Air side outlet temperature	880	°C
Operational voltage	0.731	V
Chemical-to-Electric efficiency	49.4 (1st law, LHV based)	%
Current density	2500	A/m <sup>2</sup>
<i>SOEC operation mode</i>		
Fuel side inlet temperature	820	°C
Air side inlet temperature	820	°C
Fuel side outlet temperature	777	°C
Air side outlet temperature	777	°C
Operational voltage	1.262	V
Electric-to-chemical efficiency	87.5 (1st law, LHV based)	%
Current density	2500	A/m <sup>2</sup>

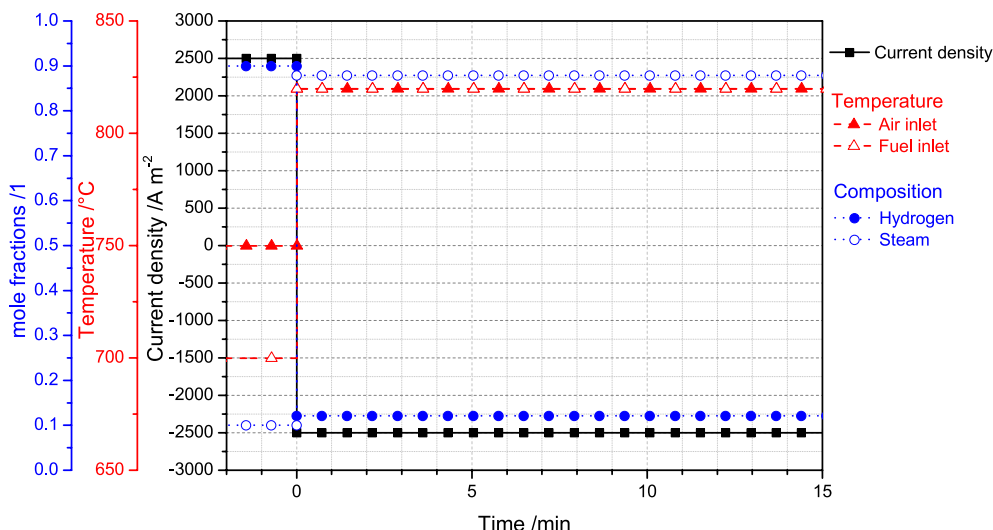


Fig. 7. Variation of the inlet conditions as a step function from SOFC operation to SOEC operating points.

maximum outlet temperature of 880 °C was reached during the SOFC operation. The electric heater was not used during the SOFC mode since enough heat was available in the product streams to preheat the inlet streams to the required temperature. In the SOEC mode, at the steady state design point, the system operates at an electric-to-chemical conversion efficiency (1st law, LHV based) of 87.5% with a steam conversion of 87%. The SOEC process is slightly endothermic resulting in an outlet temperature of 777 °C. Hence, the product streams do not have the necessary heat to preheat the inlet streams. The electric heater is used during the SOEC mode to supply the remaining heat required for preheating and for supporting the slightly endothermic SOEC operation. The power consumption of electric heat accounts for 21.8% of the chemical energy (based on LHV) produced in the form of hydrogen (which is equivalent to 25% of electrical energy consumed by rSOC excluding the BoP consumption) during the SOEC process.

The variation of the MEA temperature, local thermodynamic voltage and operational voltage along the flow direction for an SRU in the rSOC reactor at design points in SOFC and SOEC mode is shown in Fig. 10a and b. During the SOFC operation (Fig. 10a) thermodynamic voltage ( $U_{id}$ ) decreases along the flow direction due to the increase in temperature and reducing concentration of the reactants along the flow direction. The voltage loss ( $\Delta U$ ) along the length of the flow channel

mirrored the behavior of thermodynamic voltage. The higher temperatures along the reactor length resulted in lower ohmic losses along reactor length and coupled with decreasing current density along the reactor length, we observe a decreasing voltage loss along the reactor length. The voltage losses and ideal voltage distribution resulted in SRU voltage of 0.731 V. During the SOEC operation (Fig. 10b) a slightly similar behavior is observed. The thermodynamic voltage ( $U_{id}$ ) increases along the length of the reactor. This is partly due to the reducing temperature and mostly due to an increasing hydrogen concentration along the reactor length. The voltage loss ( $\Delta U$ ) decreases along the reactor length even though the temperature decreases along the reactor length. The temperature gradient is not steep along the reactor length therefore; the local ASR variation along the reactor length is not steep. But the voltage loss behavior can be explained by the distribution of local current density. The H<sub>2</sub>O concentration is higher near the inlet of the reactor resulting in a higher reaction rate and hence higher local current density near the inlet. The high local current density at the inlet results in higher voltage losses at the inlet. The reaction rate is much lower near the reactor exit resulting in low local current density and hence lower voltage losses close to the reactor exit.

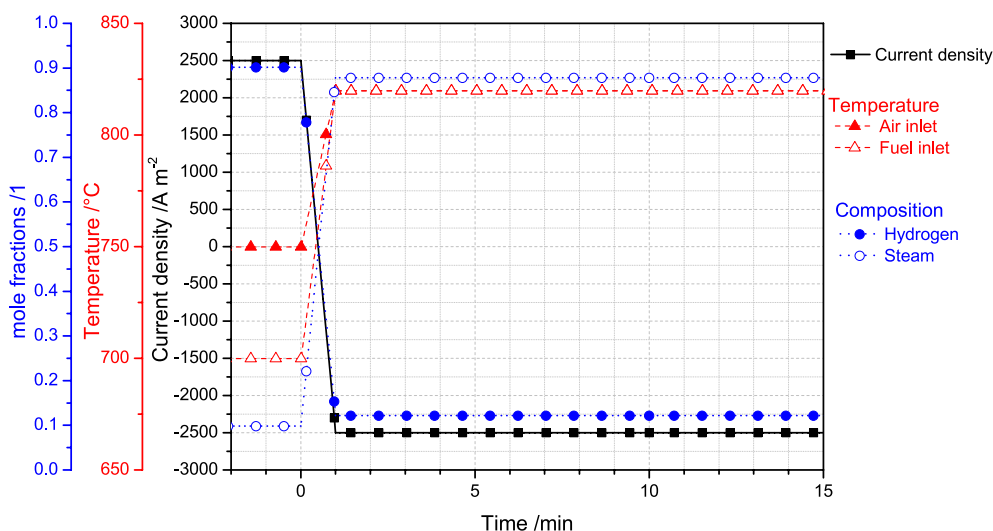


Fig. 8. Variation of the inlet conditions as a ramp function from SOFC operation condition to SOEC operation. Inlet gas temperatures, gas compositions are changed in time duration of 1 min.

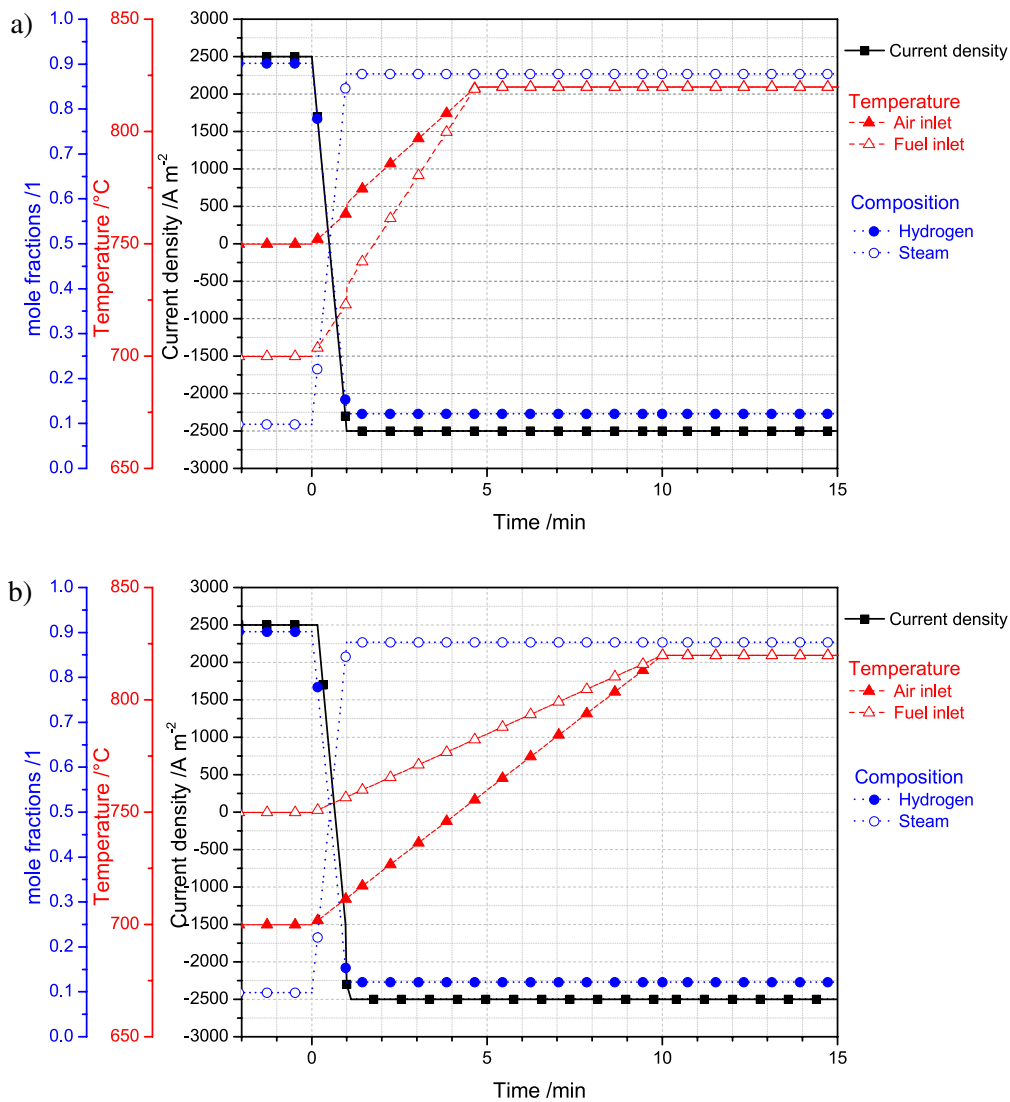


Fig. 9. Variation of the inlet conditions as a ramp function from SOFC to SOEC mode. Current and compositions are changed in 1 min duration; (a) Inlet temperatures are changed in duration of 5 mins, (b) Inlet temperatures are changed in duration of 10 mins.

5.3.2. rSOC reactor behavior during transient operation

The voltage response to the mode change for the different transient operation is shown in Fig. 11 and further discussed. The behavior of the MEA temperature to the different transient operations at different locations along the flow direction is discussed. The temperature changes for different transient operation scenarios are depicted as contour plots in Fig. 12.

5.3.2.1. Voltage response. A step function transient operation between the SOFC and SOEC operation point is studied. In reality, such a transient operation is difficult to achieve due to possible limitations of the balance of plant components as explained in the previous section. In Fig. 11 the voltage response for the operation switch (black line) is shown. The voltage response to the change in current density and operation mode is rapid. The voltage changes from 0.731 V at the SOFC

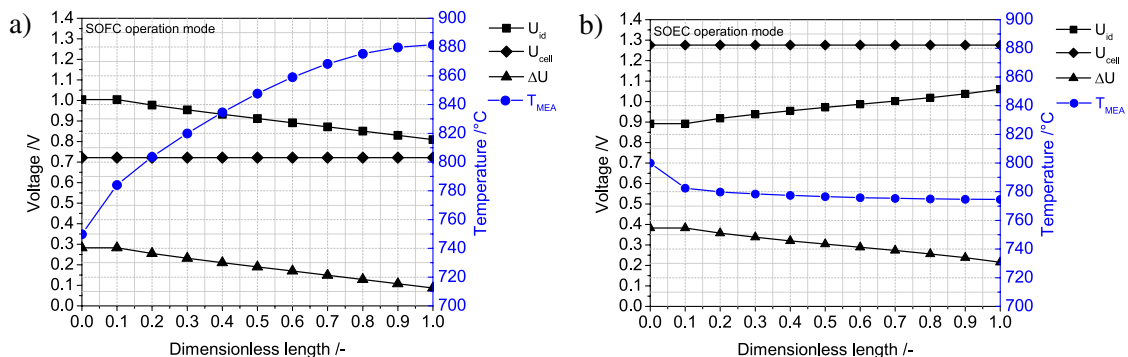


Fig. 10. Variation of temperature, ideal voltage and losses in SRU at system operation conditions with current density at 2500 A/m<sup>2</sup> and 1 bar pressure in (a) SOFC operation mode and (b) SOEC operation mode.

steady state point to 1.15 V in 1.5 min and gradually attains a steady state SOEC operational voltage of 1.26 V in 30 min. The rate of the change in the operational voltage more or less matches the rate at which the current density is varied from the SOFC mode to the SOEC mode. A similar behavior can be observed for the other transient operation strategies as well. From the observations, it can be stated that the voltage response of the rSOC reactor to the operation change is fast and matches the rate of the change in current. It must be pointed out that, for all the cases observed, the reactant composition and mass flows were varied accordingly. They should either match or should be faster than the change in current density. Under any circumstance, if the response of the reactant flows is slower than the current density variation, the voltage will not respond as observed and in most cases will lead to reactant undersupply effects in the rSOC reactor. Hence for system operation, the transition strategy presented in Simulation #1 is not viable since a step function for the variation of temperature and gas flows are impossible to achieve.

**5.3.2.2. Temperature response along the flow direction.** In Fig. 12, the spatial and temporal variation of the MEA temperature (contour plot) along the reactor length (y-axis) with time (x-axis) is shown for the different simulations. The temporal temperature changes are discussed for two spatial locations.

**5.3.2.3. Temperature response near reactor inlet.** The steady state temperature during the SOFC operation was 785 °C near the inlet of the SRU. For the SOEC operation, the reactants' inlet temperature is raised to 820 °C as a step function for simulation #1. The temperature change for this condition is shown in Top left of Fig. 12. For the simulation #1, a sharp increase of 10 °C in the temperature in less than 0.5 min near the inlet of the rSOC reactor is observed. This corresponds to a slope of at least 20 K/min. Such steep increase in temperature in a short of span of time can be critical for the rSOC reactor. It could induce a sharp thermal stress which may lead to eventual failure and reduce system operational lifetime. The temperature then gradually approaches a temperature of 783 °C. This corresponds to a steady state temperature close to the inlet of the rSOC reactor at the steady state SOEC operating point as seen from Fig. 10b. A similar temperature behavior (gradient of 18 °C/min) is observed for the Simulation #2 (Fig. 12: Top Right), where the inlet reactant compositions, temperature and current density are varied as a ramp function for equal ramp duration of 1 min. Hence, the transition strategy presented by Simulation #1 and Simulation #2 are critical and may lead to reactor failure.

In order to reduce the gradient near the inlet of the rSOC reactor, a more gradual increase of inlet temperature was chosen. In Simulation #3, the reactant inlet temperature is gradually increased from the SOFC operating point to the SOEC operating point. The duration for the temperature increase is 5 min and 10 min for Simulation #3a and Simulation #3b respectively. The temperature gradient (K/min) decreased for Simulation #3a (Fig. 12; bottom left) and #3b (Fig. 12; bottom right) respectively. This translates to a decreased temperature gradient of 5 K/min and less than 1 K/min for Simulation #3a and #3b respectively, which is within the acceptable limits for the given rSOC reactor. For simulation #3b the temperature gradient is barely significant.

**5.3.2.4. Temperature response from mid to outlet of reactor.** The temporal behavior of the MEA temperature from middle (dimensionless length of 0.5) to outlet (dimensionless length of 1) of the SRU for the different transient operation strategies is shown in Fig. 12. The temperatures in these regions are initially at 847 °C (near the middle) to 880 °C (near the outlet) which are the temperatures at the steady state SOFC operating point. During transition from the SOFC mode to the steady state SOEC operating point the MEA temperature decreases and approaches the steady state temperature of 758 °C. The highest local temperature

gradient in this region is about -15 K/min for all the transition strategies considered which is within the acceptable range for the given rSOC reactor. If required, the local temporal temperature gradient can be further reduced to less than -15 K/min by controlling the air flow rate in the reactor. The profile of the temperature variation is more or less the same for all the three different transient operation strategies. Simulations #3a and #3b attain the steady state SOEC temperature of 785 °C within 15 mins.

## 6. Summary

Using a 1-D SOC reactor model a simple hydrogen based rSOC system was developed to investigate behavior during the mode switch. The simple design leads to a system efficiency of 49% in SOFC mode and 87% in SOEC mode, resulting in a roundtrip efficiency of 42%. The behavior of the rSOC reactor during the operational switch was analyzed. The effect of three different transition strategies on the temperature profile along the length of the rSOC reactor and the voltage response was studied. The study was performed for the switching from an SOFC operating point to an SOEC operating point. From the analysis, a rapid switch is possible from an electrochemical perspective. The voltage response to the operation change is fast. But, this comes with a caveat that the reactant flows (mass flow and compositions) to the rSOC reactor should also vary equally fast. Therefore for the conditions considered in this analysis, a step function switch for the reactant flows is not realistically possible. Hence, the transient operation represented in Simulation #1 is not feasible. Additionally, a step function transient behavior as used in Simulation #1 is detrimental since it induces a sharp temperature increase near the inlet of the rSOC reactor. To accommodate the time required for switching the reactant flows from the SOFC to those required for SOEC operating point, a ramp function is considered. In Simulation #2 and Simulation #3 a ramp function is considered where the reactant flows and operation mode are switched in a duration of 1 min. In Simulation #2, the inlet temperature of the reactants changes as a ramp function within a duration of 1 min. This still leads to a temperature spike near the inlet which can be damaging to the rSOC reactor. Of the three scenarios analyzed, Simulation #3 presents the most feasible solution. Here the reactant flows are still switched from SOFC operation to those required for SOEC operation in the short duration of 1 min but the temperature change is given much more time. To enable such quick operational switching, modifications in the process system may be required. These include a backup steam generator as a buffer, to provide steam required for the electrolysis operation since steam generation is generally a sluggish process. Higher inlet temperatures are used in the electrolysis process to support

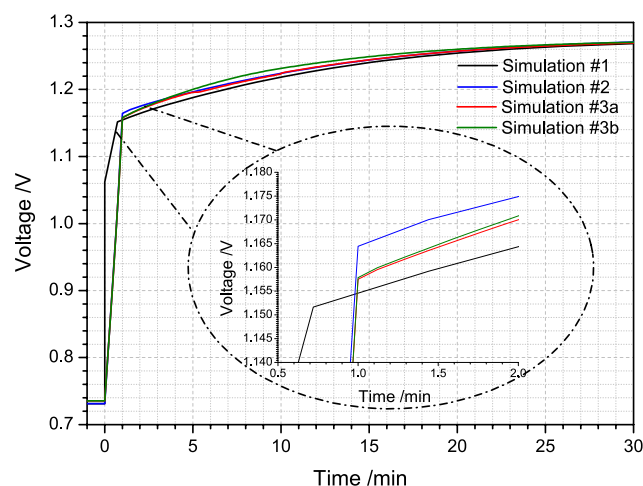


Fig. 11. Behavior of the rSOC operational voltage to the load and operation mode variation for different transient operation.

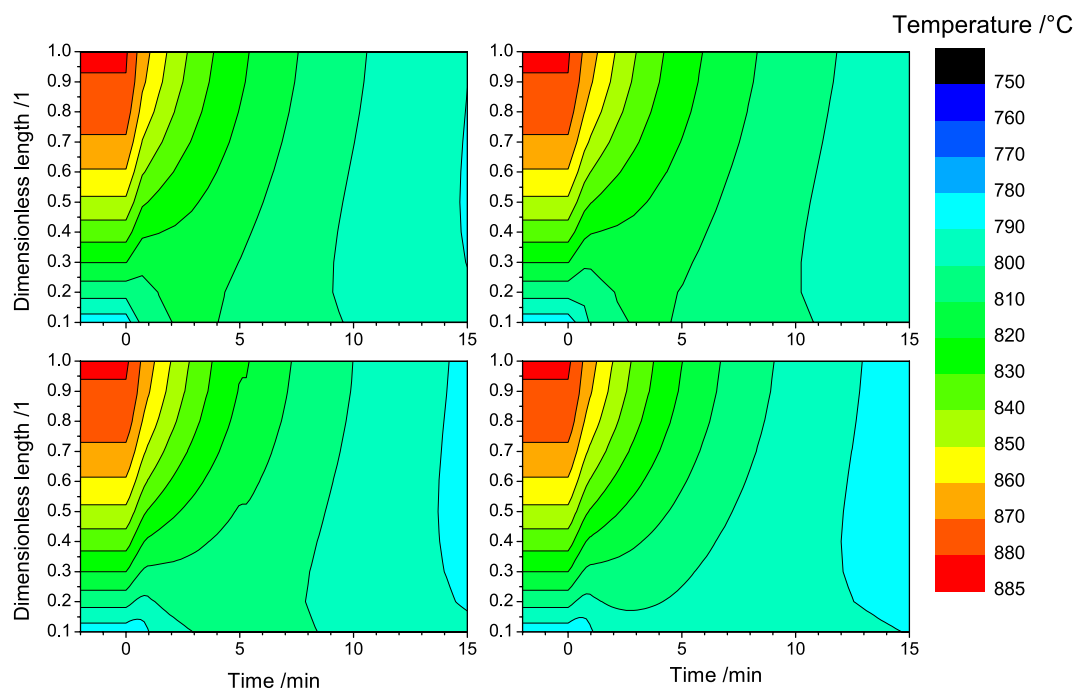


Fig. 12. Response of MEA solid temperature along the flow direction for different transient operation scenarios; Top Left: Simulation #1, Top Right: Simulation #2, Bottom Left: Simulation #3a and Bottom Right: Simulation #3b.

endothermic behavior, from the analysis it is shown that the inlet temperature can increase gradually from the SOFC operation point to the SOEC operation point. The temperature change can be an order of magnitude slower than the change in reactant flows and operation mode. The above analysis will be used as a basis to develop optimal control concepts for the system and optimize the process system. The results presented in this work will lay the foundation for development control strategies of the system, optimization of BoP components and control which would then be used in the future projects where a prototype will be built in cooperation with industrial partners.

## 7. Conclusions and outlook

- In this paper, a 1-D model of a single repeat unit in an rSOC reactor was developed for process system analysis. The 1-D model was implemented in an open source object oriented programming language; Modelica using the commercial Dymola editor. The model was further validated in both SOFC and SOEC operation modes based on experimental characterization of a commercially available rSOC reactor.
- A simple hydrogen based rSOC system model was built employing a validated 1-D rSOC reactor model to investigate transient reactor operation where the SOEC process was operated in a slightly endothermic region. The simple design leads to a system efficiency of 49% and 87% in the steady state SOFC and SOEC design points respectively.
- The voltage response to load and operation change is rapid. This due to the fact that the electrochemical reactions are generally fast reactions, provided that the reactants supply to the rSOC reactor is also varied fast enough. For the system considered in this analysis, the reactants vary from 90 mol% hydrogen and 10 mol% water in the SOFC mode to 12 mol% hydrogen and 88 mol% water in the SOEC operation mode. Therefore the change in composition of the reactants and corresponding mass flows for the different operation points should respond quickly to the operation change. Based on this criterion alone, a step change from SOFC to SOEC or vice versa is not feasible in a system context due to BoP component behavior. Hence a fast ramp function is preferred where the operation changes from

SOFC to SOEC mode in the duration of 1 min.

- Due to endothermic operation of the SOEC process, the rSOC inlet temperatures of the reactants are higher than that used for exothermic SOFC operation. The inlet temperatures vary from 750 °C in SOFC operation to 820 °C in SOEC operation for the fuel flow and 700 °C in SOFC operation to 820 °C in SOEC operation for the air flow. From the analysis presented, it can be concluded that temperature can vary slower than the change in operation mode and is in fact advantageous. It was shown that the temperature change can and should be 10 times slower than operation change. This is to ensure the rSOC reactor is kept “happy” from temperature perspective at all points of operation; SOFC mode, SOEC mode and during transient operation from SOFC to SOEC mode.
- To enable the quick transition between the operation modes, the results from the current analysis of reactor behavior will be used as a basis to optimize the control strategy of the system, identify appropriate balance of plant components and optimize the dynamic response of the balance of plant components in the following work. The supply of the reactants to the rSOC reactor should respond quickly to the change in operation mode, especially steam generation in the SOEC operation mode. Hence, an additional steam buffer system or electric steam generator is proposed to buffer the immediate steam requirements.

## Acknowledgements

I would like to thank Marc Riedel for sharing the experimental results for the model validation and for his valuable discussion on evaluating the fit parameters for the model.

## References

- [1] Dell RM, Rand DAJ. Energy storage – a key technology for global energy sustainability. *J Power Sources* 2001;100:2–17.
- [2] Hemmes K, Guerrero JM, Zhelev T. Highly efficient distributed generation and high-capacity energy storage. *Chem Eng Process: Process Intensif* 2012;51:18–31.
- [3] Mottaghizadeh P, Santhanam S, Heddrich MP, Friedrich KA, Rinaldi F. Process modeling of a reversible solid oxide cell (r-SOC) energy storage system utilizing commercially available SOC reactor. *Energy Convers Manag* 2017;142:477–93.

- [4] Jensen SH, et al. Large-scale electricity storage utilizing reversible solid oxide cells combined with underground storage of CO<sub>2</sub> and CH<sub>4</sub>. *Energy Environ Sci* 2015.
- [5] Monti A, Wendel CH, Santarelli M, Braun RJ. Energy dense storage using intermediate temperature reversible solid oxide cell systems. *ECS Trans* 2015;68(1):3289–300.
- [6] Frank M, Deja R, Peters R, Blum L, Stolten D. Bypassing renewable variability with a reversible solid oxide cell plant. *Appl Energy* 2018;217(February):101–12.
- [7] Li M, Brouwer J, Rao AD, Samuelsen GS. Application of a detailed dimensional solid oxide fuel cell model in integrated gasification fuel cell system design and analysis. *J Power Sources* 2011;196(14):5903–12.
- [8] Magistri L, Bozzo R, Costamagna P, Massardo AF. Simplified versus detailed solid oxide fuel cell reactor models and influence on the simulation of the design point performance of hybrid systems. *J Eng Gas Turbines Power* 2004;126(July):516–23.
- [9] Harun NF, Shadle L, Oryshchyn D, Tucker D. Fuel utilization effects on system efficiency and solid oxide fuel cell performance in gas turbine hybrid systems. *Proc ASME Turbo Expo* 2017;3(July):1953–65.
- [10] Achenbach E. Three-dimensional and time-dependent simulation of a planar solid oxide fuel cell stack. *J Power Sources* 1994;49(1–3):333–48.
- [11] Menon V, Janardhanan VM, Tischler S, Deutschmann O. A novel approach to model the transient behavior of solid-oxide fuel cell stacks. *J Power Sources* 2012;214:227–38.
- [12] Laurencin J, Kane D, Delette G, Deseure J, Lefebvre-Joud F. Modelling of solid oxide steam electrolyser: impact of the operating conditions on hydrogen production. *J Power Sources* 2011;196(4):2080–93.
- [13] Ni M. 2D thermal modeling of a solid oxide electrolyzer cell (SOEC) for syngas production by H<sub>2</sub>O/CO<sub>2</sub> co-electrolysis. *Int J Hydrogen Energy* 2012;37(8):6389–99.
- [14] Iora P, Aguiar P, Adjiman CS, Brandon NP. Comparison of two IT DIR-SOFC models: Impact of variable thermodynamic, physical, and flow properties. Steady-state and dynamic analysis. *Chem Eng Sci* 2005;60(11):2963–75.
- [15] Aguiar P, Adjiman CS, Brandon NP. Anode-supported intermediate temperature direct internal reforming solid oxide fuel cell. I: Model-based steady-state performance. *J Power Sources* 2004;138(1–2):120–36.
- [16] Udagawa J, Aguiar P, Brandon NP. Hydrogen production through steam electrolysis: model-based steady state performance of a cathode-supported intermediate temperature solid oxide electrolysis cell. *J Power Sources* 2007;166(1):127–36.
- [17] Salogni a, Colonna P. Modeling of solid oxide fuel cells for dynamic simulations of integrated systems. *Appl Therm Eng* 2010;30(5):464–77.
- [18] Kazempour P, Braun RJ. Model validation and performance analysis of regenerative solid oxide cells for energy storage applications: reversible operation. *Int J Hydrogen Energy* 2014;39(11):5955–71.
- [19] Jin X, Xue X. Mathematical modeling analysis of regenerative solid oxide fuel cells in switching mode conditions. *J Power Sources* 2010;195(19):6652–8.
- [20] Hajimolana SA, Hussain MA, Daud WMAW, Soroush M, Shamiri a. Mathematical modeling of solid oxide fuel cells: a review. *Renew Sustain Energy Rev* 2011;15(4):1893–917.
- [21] Mogensen D, Grunwaldt J-D, Hendriksen PV, Dam-Johansen K, Nielsen JU. Internal steam reforming in solid oxide fuel cells: status and opportunities of kinetic studies and their impact on modelling. *J Power Sources* Jan. 2011;196(1):25–38.
- [22] Xu J, Froment GF. Methane steam reforming, methanation and water-gas shift: I. Intrinsic kinetics. *AIChE J* 1989;35(1):88–96.
- [23] Achenbach E, Riensche E. Methane/steam reforming kinetics for solid oxide fuel cells. *J Power Sources* 1994;52(2):283–8.
- [24] Wang Y, Yoshida F, Kawase M, Watanabe T. Performance and effective kinetic models of methane steam reforming over Ni/YSZ anode of planar SOFC. *Int J Hydrogen Energy* May 2009;34(9):3885–93.
- [25] Hecht ES, et al. Methane reforming kinetics within a Ni-YSZ SOFC anode support. *Appl Catal A Gen* 2005;295:40–51.
- [26] Lehnert W, Meusinger J, Thom F. Modelling of gas transport phenomenon in SOFC anodes. *J Power Sources* 2000;87:57–63.
- [27] Timmermann H, Sawady W, Reimert R, Ivers-Tiffée E. Kinetics of (reversible) internal reforming of methane in solid oxide fuel cells under stationary and APU conditions. *J Power Sources* 2010;195(1):214–22.
- [28] Santhanam S, Heddrich MP, Riedel M, Friedrich KA. Theoretical and experimental study of Reversible Solid Oxide Cell (r-SOC) systems for energy storage. *Energy* 2017;141:202–14.
- [29] Colpan C. A review on macro-level modeling of planar solid oxide fuel cells. *Int J* 2008;336–55.
- [30] Noren DA, Hoffman MA. Clarifying the Butler-Volmer equation and related approximations for calculating activation losses in solid oxide fuel cell models. *J Power Sources* 2005;152:175–81.
- [31] Ferrero D, Lanzini A, Leone P, Santarelli M. Reversible operation of solid oxide cells under electrolysis and fuel cell modes: experimental study and model validation. *Chem Eng J* 2015;274:143–55.
- [32] García-Camprubí M, Izquierdo S, Fueyo N. Challenges in the electrochemical modelling of solid oxide fuel and electrolyser cells. *Renew Sustain Energy Rev* 2014;33:701–18.
- [33] Suwanwarangkul R, Croiset E, Fowler MW, Douglas PL, Entchev E, Douglas MA. Performance comparison of Fick's, dusty-gas and Stefan-Maxwell models to predict the concentration overpotential of a SOFC anode. *J Power Sources* 2003;122(1):9–18.
- [34] Fu Y, et al. Multicomponent gas diffusion in porous electrodes. *J Electrochem Soc* 2015;162(6):F613–21.
- [35] Bhattacharyya D, Rengaswamy R. A review of Solid Oxide Fuel Cell (SOFC) dynamic models. *Ind Eng Chem Res* 2009;48(13):6068–86.
- [36] Henke M, Kallo J, Friedrich KA, Bessler WG. Influence of pressurisation on SOFC performance and durability: a theoretical study. *Fuel Cells* 2011;11(4):581–91.
- [37] Wang Y, Yoshida F, Watanabe T, Weng S. Numerical analysis of electrochemical characteristics and heat/species transport for planar porous-electrode-supported SOFC. *J Power Sources* 2007;170(1):101–10.
- [38] Magar YN, Manglik RM. Modeling of convective heat and mass transfer characteristics of anode-supported planar solid oxide fuel cells. *J Fuel Cell Sci Technol* 2007;4(2):185.
- [39] Vayenas CG, Debenetti PG, Yentekakis I, Hegedus LL. Cross-flow, solid-state electrochemical reactors: a steady state analysis. *Ind Eng Chem Fundam* 1985;24(3):316–24.
- [40] Brus G, Szymid J. Numerical modelling of radiative heat transfer in an internal indirect reforming-type SOFC. *J Power Sources* 2008;181(1):8–16.
- [41] VanderSteen JJJ, Pharoah JG. Modeling radiation heat transfer with participating media in solid oxide fuel cells. *J Fuel Cell Sci Technol* 2006;3(1):62.
- [42] Damm DL, Fedorov AG. Radiation heat transfer in SOFC materials and components. *J Power Sources* 2005;143(1–2):158–65.
- [43] Riedel M, Heddrich MP, Friedrich KA. Pressurized operation of a 10 layer solid oxide electrolysis stack. In: 12th European SOFC & SOE Forum, 2016, vol. 911, no. July .p. 97–101.
- [44] Ghatee M, Shariat MH, Irvine JTS. Investigation of electrical and mechanical properties of 3YSZ/8YSZ composite electrolytes. *Solid State Ionics* 2009;180(1):57–62.
- [45] Weber A, Ivers-Tiffée E. Materials and concepts for solid oxide fuel cells (SOFCs) in stationary and mobile applications. *J Power Sources* 2004;127(1–2):273–83.
- [46] Leonide a, Apel Y, Ivers-Tiffée E. SOFC modeling and parameter identification by means of impedance spectroscopy. *ECS Trans* 2009;19(20):81–109.
- [47] Leonide A, Sonn V, Weber A, Ivers-Tiffée E. Evaluation and modeling of the cell resistance in anode-supported solid oxide fuel cells. *J Electrochem Soc* 2008;155(1):B36.